Rarefaction and Compressibility Effects in Gas Microflows

Ali Beskok
Research Associate.

George Em Karniadakis
Professor.

Center for Fluid Mechanics,
Brown University,
Providence, RI 02912

William Trimmer
President of Belle Mead Research, Inc.,
Belle Mead, NJ 08502

Gas microflows are encountered in many applications of Micro-Electro-Mechanical Systems (MEMS). Computational modeling and simulation can provide an effective predictive capability for heat and momentum transfer in microscales as well as means of evaluating the performance of a new microdevice before hardware fabrication. In this article, we present models and a computational methodology for simulating gas microflows in the slip-flow regime for which the Knudsen number is less than 0.3. The formulation is based on the classical Maxwell/Smoluchowski boundary conditions that allow partial slip at the wall. We first modify a high-order slip boundary condition we developed in previous work so that it can be easily implemented to provide enhanced numerical stability. We also extend a previous formulation for incompressible flows to include compressibility effects which are primarily responsible for the nonlinear pressure distribution in microchannel flows. The focus of the paper is on the competing effects of compressibility and rarefaction in internal flows in long channels. Several simulation results are presented and comparisons are provided with available experimental data. A specific set of benchmark experiments is proposed to systematically study compressibility, rarefaction and viscous heating in microscales in order to provide validation to the numerical models and the slip-flow theory in general as well as to establish absolute standards in this relatively young field of fluid mechanics.

1 Introduction

Micron size mechanical devices are becoming more prevalent, both in commercial applications and in scientific inquiry. Small accelerometers, with dimensions measured in microns, are being used to deploy air bag systems in automobiles. Tiny pressure sensors for the tip of a catheter are smaller than the head of a pin. Micro actuators are moving scanning electron microscope tips to image single atoms. New fabrication techniques, such as surface silicon micromachining, bulk silicon micromachining, LIGA (Lithographie Galvanoformung Abformung), and EDM (Electro Discharge Machining) are making these microdevices possible. The capability to batch fabricate and automate these fabrication technologies makes these microdevices inexpensive (Howe et al., 1990; Bryzek et al., 1994; Reed, 1993). Inherent with these new technologies is the need to develop fundamental science and engineering of small devices. Microdevices tend to behave differently than the objects we are used to handling in our daily life. The inertial forces, for example, tend to be quite small and surface effects tend to dominate their behavior. Friction, electrostatic forces, and viscous effects due to the surrounding air or liquid become increasingly important as the devices become smaller.

This paper focuses on the fundamental laws and the metrology of gas microflows, i.e., gas flows in devices with characteristic dimension of the order of a micron (μm). They are encountered in many applications of Micro-Electro-Mechanical Systems (MEMS) such as instrumentation, microelectronics, bioengineering, and advanced energy systems (Gabriel et al., 1988; O'Connor, 1992). An example of such a device is a polysilicon, surface-micromachined side-drive micromotor. The fabrication, operation, and performance of such a motor have been studied extensively in recent years by Tai et al. (1989), and Mehregany et al. (1990). Figure 1 shows a sketch of such a motor along with the characteristic dimensions. Typical operating conditions for an angular speed of $\omega = 5000$ rad/sec show that the Reynolds number $\mathrm{Re} \simeq 1$ for the flow in the gap and that the Mach number $\mathrm{M} < 0.01$ based on the rotor tip speed. In this small gap, a gas flow cannot be modeled based on the continuum hypothesis. The deviation of the state of the gas from continuum is measured by the Knudsen number (Kn), which is defined as $\mathrm{Kn} = \lambda/L$, where λ is the mean free path of the molecules and L is representative of the domain length. For this micromotor, using the rotor base dimensions ($L = 3$ μm) and assuming that operation conditions are atmospheric, we obtain the value $\mathrm{Kn} = 0.022$.

While the nominal Knudsen number is relatively small for the above example, there are other applications of microflows where the Knudsen number is significantly larger. For example, in magnetic disk storage, the gap between the magnetic head and the recording medium varies from 0.2 to 0.05 μm with the smaller dimension corresponding to an increase in recording capacity. The Knudsen number in this case is above one. Similarly, other microflows such as flows in helium leak detection microdevices and mass spectrometers correspond to a Knudsen number that may achieve values up to 200 (Tison, 1993).

As the value of Knudsen number increases, rarefaction effects become more important and thus pressure drop, shear stress, heat flux and corresponding mass flowrate cannot be predicted from flow and heat transfer models based on the continuum hypothesis. On the other hand, simple models based on kinetic gas theory concepts are not appropriate either. An exception is the very high Knudsen number regime corresponding to near vacuum conditions in finite size devices or at atmospheric conditions but at device dimensions of the order of nanometer (nm). The appropriate flow and heat transfer models depend on the range of the Knudsen number. A classification of the different flow regimes is as follows (Schaaf and Chambre, 1961): For $\mathrm{Kn} \leq 10^{-3}$ the fluid can be considered as a continuum, while for $\mathrm{Kn} \geq 10$ it is considered a free molecular flow. A rarefied gas can neither be considered an absolutely continuous medium nor a free-molecule flow in the Knudsen number range between 10^{-3} and 10. In that region, a further classification is needed, i.e., slip-flow ($10^{-3} < \mathrm{Kn} < 0.1$) and transition flow ($0.1 < \mathrm{Kn} < 10$). This classification is based on empirical

Contributed by the Fluids Engineering Division for publication in the JOURNAL OF FLUIDS ENGINEERING. Manuscript received by the Fluids Engineering Division March 17, 1995; revised manuscript received March 26, 1996. Associate Technical Editor: D. P. Telionis.

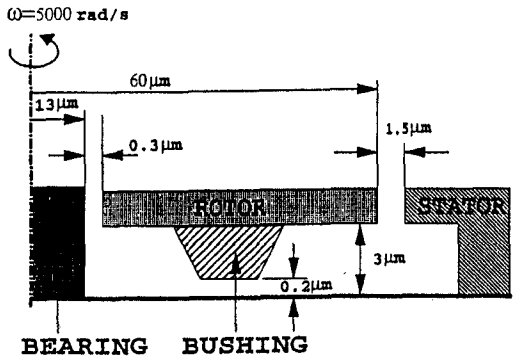

Fig. 1 Diagram of a side-driven micromotor with typical dimensions

information and thus the limits between the different flow regimes may depend on the problem geometry and special conditions. A comprehensive review on the theory of internal flows at low pressures is given by Thompson and Owens (1975); a general review on rarefied gas dynamics is given by Muntz (1989).

A verification of this taxonomy is provided in Fig. 2 where we plot the experimental data by S. Tison obtained at the National Institute of Standards (NIST) at very low pressures in a pipe of diameter $d = 2$ mm (Tison, 1994). Both inlet and outlet pressures were varied in the experiment while the corresponding Knudsen number varied from almost 0 to 200. In this log-log plot, we can easily identify three distinct flow regimes, although the corresponding values at the boundaries between the different regimes is somewhat different than the aforementioned ones (Schaaf and Chambre, 1961). In particular, the slip flow regime extends up to Kn = 0.6 and the transition regime up to Kn = 17. It is interesting to notice the very slow variation of mass flowrate in terms of the pressure difference in the transition regime. In that range of Knudsen number a minimum occurs in the mass flowrate divided by the difference of inlet and exit pressures ($\dot{M}/\Delta P$) if the data are replotted in terms of the average pressure between inlet and outlet. This minimum was first identified by Knudsen (1909) and has been observed in many experimental and analytical studies (Tison, 1993; Loyalka and Hamoodi, 1990; (see Kennard, 1938 p. 309). The form of the plot in Figure 2 also suggests that a nonlinear pressure drop takes place in this rarefied pipe flow. Scaling of the mass flowrate with the difference of pressure squares is characteristic of low Reynolds number, *compressible* flows in long channels.

The first experimental study of microflows using micro-machined channels was conducted for both gases and liquids by Pfahler et al. (1991) in a Reynolds number range $0.50 \leq Re \leq 20$ and Knudsen number $0.001 \leq Kn \leq 0.363$ for a hydraulic channel diameter $D_h = 8$ μm and channel length 11 mm. The corresponding Mach number at the inlet was very small but at the exit high subsonic values were achieved. For example, for an inlet to exit pressure ratio of 10, exit Mach numbers as high as 0.7 are reported by Pfahler et al. (1991) and Harley et al. (1995). The reported skin friction reduction due to apparent slip of the flow has been confirmed in other similar experimental studies (Arkilic et al., 1994) using different microfabrication techniques to fabricate the microchannels. In particular, in the work of Liu et al. (1993) and Pong et al. (1994) the pressure distribution along the microchannel was measured by using a surface micromachined system with a number of sensors as part of the surface. A nonlinear pressure distribution was clearly demonstrated in these experiments; however more data are needed to adequately describe its origin. Other recent work focusing on measuring and modeling microflows is presented in Shoji and Esashi (1994), Wilding et al. (1994), and Zengerle and Richter (1994).

In our studies we have identified four important effects in microflows. These are: *compressibility, rarefaction, viscous heating, and thermal creep effects.* The current paper emphasizes compressibility and rarefaction effects for shear and pressure driven microflows. Viscous heating is due to the work done by viscous stresses, and it is important for microflows, especially in creating temperature gradients within the domain even for isothermal boundary conditions. The thermal creep (transpiration) phenomenon is a rarefaction effect. For rarefied gas flows it is possible to start the motion with tangential temperature gradients along the channel surface. In such a case the gas molecules start creeping from cold to hot direction (Kennard, 1938, Kruger et al., 1970). Thermal creep can be important in causing variation of pressure along tubes in the presence of tangential temperature gradients. Thermal creep effects are also included in our model; the importance of these effects for incompressible flows has been documented in Beskok and Karniadakis (1994). A systematic study of thermal creep for compressible flows will be presented in a future publication.

Numerical simulation studies are well suited for microflows, however the breakdown of continuum at microscales leads to uncertainties regarding the governing constitutive laws. In the slip-flow regime, it is reasonable to employ the Navier-Stokes equations modified at the surface with appropriate velocity-slip conditions (Thompson and Owens, 1975). In previous work, in a series of papers (Beskok and Karniadakis, 1992, 1993, 1994) we developed an incompressible flow model with high-order velocity-slip boundary conditions. This approach essentially extends the governing equations used in modeling high-altitude slightly rarefied aerodynamic flows (Kennard, 1938; Schaaf and Chambre, 1961). In the current work, we use a numerical formulation we have developed for *compressible* no-slip as well as slip-flows in order to quantify the compressibility and rarefaction effects in the slip-flow regime. The results we present are consistent with experimental studies and agree very well in nondimensional form both for flows in microdomains where the Knudsen number is finite, due to the micron-size characteristic length, as well as in flows in domains of large size at near vacuum conditions. A fundamental question concerns the validity of the *dynamical similarity* between these two types of flows. In other words, are microflows at atmospheric conditions dynamically similar to rarefied (i.e., low pressure) flows in macro-domains. In conjunction with such questions we propose a set of benchmark experiments which, we believe, will aid in our fundamental understanding of the flow physics

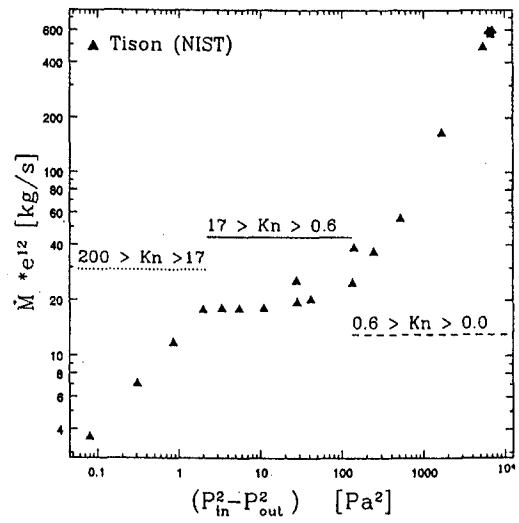

Fig. 2 Variation of mass flowrate as a function of $(P_{in}^2 - P_{out}^2)$. The data are for rarefied gas flow experiments conducted by S. Tison at NIST (Kn is based on the pipe exit pressures which are very close to vacuum, and pipe radius).

and will validate the computational models we develop in this work.

The paper is organized as follows: In Section 2 we summarize the mathematical and numerical formulation and develop a high-order velocity slip boundary condition. In Section 3 we present typical results in shear-driven flows and compare with analytical models. In Section 4 we include results for pressure-driven flows and compare with experimental results. In Section 5 we propose a set of benchmark experiments motivated by the simulation results. Finally, in Section 6 we summarize our findings.

2 Models and Formulation

2.1 Compressible Navier-Stokes Algorithm. We consider here the slip-flow regime where we assume that gas microflows are governed by the Navier-Stokes equations and appropriate velocity-slip boundary conditions. In a previous study (Beskok and Karniadakis, 1994), we developed an incompressible flow formulation; however, the experimental results reported by Liu et al. (1993) show nonlinear pressure distribution in microchannel experiments suggestive of strong compressibility effects. For this reason, we have developed a new algorithm that solves the compressible Navier-Stokes equations using a spectral element/time-splitting algorithm. The algorithm treats the inviscid part (Euler equations) first using the characteristic decomposition procedure and a Gauss-Lobatto-Legendre collocation algorithm. Subsequently, the viscous part is discretized using a Galerkin formulation that enforces interelemental continuity conditions. Details of the algorithm including the treatment of element interface boundary conditions as well as validation of the spectral element algorithm for subsonic compressible flows in complex geometries is presented elsewhere (Beskok and Karniadakis, 1996).

In the results that follow, a systematic study of discretization errors has been performed by p-type grid refinements (increasing the order of polynomial expansions). The discretization errors are estimated by using the global mass and momentum balances. A maximum error of 1 percent in global conservation laws is taken as an acceptable norm. It was found that continuity is satisfied with 0.05 percent error and momentum is conserved with less than 1 percent error in all cases.

2.2 Velocity-Slip and Temperature-Jump Conditions. In previous studies (Beskok and Karniadakis, 1992, 1993, 1994) with incompressible flow models we employed the velocity-slip and temperature-jump boundary conditions given in the following non-dimensional form:

$$U_g - U_w = \frac{2-\sigma_v}{\sigma_v}\frac{\mathrm{Kn}}{1-b\,\mathrm{Kn}}\frac{\partial U_s}{\partial n} + \frac{3}{2\pi}(\gamma-1)\,\mathrm{Kn}^2\,\mathrm{Re}\,\frac{\partial T}{\partial s}, \quad (1a)$$

$$T_g - T_w = \frac{2-\sigma_T}{\sigma_T}\left[\frac{2\gamma}{\gamma+1}\right]\frac{\mathrm{Kn}}{\mathrm{Pr}}\frac{\partial T}{\partial n}, \quad (1b)$$

where U_g and T_g refer to the gas velocity and temperature, respectively, and U_w and T_w are the corresponding wall quantities. Also $\partial/\partial n$ and $\partial/\partial s$ denote the normal and tangential derivatives evaluated at the surface, respectively. Here σ_v and σ_T are the accommodation coefficients of the solid surface (Saxena and Joshi, 1981), and b is a high-order slip coefficient (see Beskok and Karniadakis, 1994). The case $b = 0$ corresponds to classical Maxwell (first-order) slip boundary condition.

The numerical implementation of Eqs. (1a) and (1b) are somewhat complicated due to the mixed-type (Robin) boundary conditions. An explicit (in time) implementation of Eq. (1a) at time level $(n+1)\Delta t$ (ignoring for simplicity the temperature term) is as follows:

$$U_g^{n+1} - U_w = \sum_{i=0}^{J-1}\alpha_i\left[\frac{2-\sigma_v}{\sigma_v}\left(\frac{\mathrm{Kn}}{1-b\,\mathrm{Kn}}\right)\frac{\partial U}{\partial n}\right]_s^{n-i} + \theta(\Delta t^J), \quad (2)$$

where α_i denotes the weights necessary to obtain the time-accuracy $\theta(\Delta t^J)$ with Δt the time step, and J the order of integration rule (e.g., $J = 2$ for second-order time accuracy). However, explicit treatment of boundary conditions is an extrapolation process and thus it is numerically unstable, e.g., for high values of Knudsen number.

Through numerical experimentation, we have determined that the overall Navier-Stokes solution, with explicitly implemented velocity-slip boundary conditions, becomes unstable when the calculated slip amount $(U_g - U_w)$ at a certain time step is sufficiently large to cause a sudden change of the sign of wall vorticity, in the next time step. This empirical finding can be readily justified by considering the following argument. For a linear Couette flow (see Section 3) with driving velocity U_0 and local gas velocity U_1 at a distance (Δy) away from the wall, it is possible to approximate (to a first-order accuracy and for $\sigma_v = 1$) the slip velocity U_g as:

$$U_g - U_0 = \mathrm{Kn}\,\frac{U_1 - U_0}{\Delta y}. \quad (3)$$

For no-change in the sign of vorticity at the wall, we require that $(U_0 - U_1) > (U_0 - U_g) = -\mathrm{Kn}\,(U_1 - U_0)/\Delta y$; this is satisfied if $\Delta y > \mathrm{Kn}$ (in nondimensional form). This limit is a significant restriction, especially for spectral-based methods as the one we use in our discretization, where collocation points are clustered very rapidly close to the boundaries. Therefore, spectral and high-order methods that typically provide high-order accuracy are amenable to numerical instabilities of this form.

To circumvent this difficulty and model high-order rarefaction effects accurately, we present here a reformulation of the velocity-slip boundary condition. This will be obtained by an approximate analysis of the motion of a monatomic gas near an isothermal surface. To this end, we consider the tangential momentum flux near the surface. We then assume that approximately half of the molecules are coming from the layer of gas one mean free path (λ) away from the surface with an average tangential velocity of U_λ, while the other half of the molecules are reflected from the wall. Furthermore, we assume that σ_v of the molecules are reflected from the wall diffusively (i.e., with average tangential velocity corresponding to that of the wall), and that $(1 - \sigma_v)$ of the molecules are reflected from the wall specularly (i.e., conserving their average incoming tangential velocity U_λ). Following Schaaf and Chambre (1961), the slip velocity for isothermal surfaces is then

$$U_g = \tfrac{1}{2}[U_\lambda + (1-\sigma_v)U_\lambda + \sigma_v U_w]. \quad (4)$$

This was also our starting point in the derivation of Eq. (1a) including second-order effects (Beskok and Karniadakis, 1994). In this new approach, we first find all locations at a distance (λ) away from the surface. We then perform spectrally accurate interpolations to find the local flow variables (U_λ, T_λ) at these locations, and subsequently evaluate the slip velocity using Eq. (4).

Next we show that Eq. (4) corresponds to a high-order slip boundary condition by simply expanding U_λ in (4) in terms of U_g, using Taylor series expansion. This results in:

$$U_g - U_w = \frac{2-\sigma_v}{\sigma_v}\left[\mathrm{Kn}\left(\frac{\partial U}{\partial n}\right)_s + \frac{\mathrm{Kn}^2}{2}\left(\frac{\partial^2 U}{\partial n^2}\right)_s + \frac{\mathrm{Kn}^3}{6}\left(\frac{\partial^3 U}{\partial n^3}\right)_s + \ldots\right], \quad (5)$$

where the subscript s denotes the surface where slip occurs and n is the normal coordinate.

For the temperature-jump boundary condition, a derivation based on kinetic theory of gases is given in (Kennard, 1938). We propose the following form for the high-order temperature-jump condition by analogy with Eq. (5):

$$T_g - T_w = \frac{2-\sigma_T}{\sigma_T}\left[\frac{2\gamma}{\gamma+1}\right]\frac{1}{\mathrm{Pr}}\left[\mathrm{Kn}\left(\frac{\partial T}{\partial n}\right)_s + \frac{\mathrm{Kn}^2}{2}\left(\frac{\partial^2 T}{\partial n^2}\right)_s + \frac{\mathrm{Kn}^3}{6}\left(\frac{\partial^3 T}{\partial n^3}\right)_s + \ldots\right], \quad (6)$$

which can be re-arranged by recognizing the Taylor series expansion of T_λ about T_g to give a temperature-jump boundary condition similar to Eq. (4) as:

$$T_g = \frac{\dfrac{(2-\sigma_T)}{\mathrm{Pr}}\dfrac{\gamma}{(\gamma+1)}T_\lambda + \sigma_T T_w}{\sigma_T + \dfrac{(2-\sigma_T)}{\mathrm{Pr}}}. \quad (7)$$

If temperature gradients are present along the surface, the velocity slip is modified to include thermal creep (Kennard, 1938). Equation (4) should then include the term $(3\sigma_v/8)(\mu R/P)(\partial T/\partial s)$, where s denotes the direction along the surface.

We have found that these new boundary conditions (Eqs. (4) and (7) are numerically stable for values of Knudsen number up to 0.5, covering essentially the entire slip-flow regime. The previous boundary condition developed in (Beskok and Karniadakis, 1994) caused numerical instabilities for typical flows above $\mathrm{Kn} > 0.1$.

As regards accuracy of the two velocity-slip boundary conditions, i.e., Eq. (1a) versus Eq. (4) we can analyze the differences for the two-dimensional pressure-driven incompressible flow between parallel plates separated by a distance h in the slip-flow regime. Assuming isothermal conditions and that the slip is given by Eq. (4), the corresponding velocity distribution is

$$U(y) = \frac{h^2}{2\mu}\frac{dP}{dx}\left[\frac{y^2}{h^2} - \frac{y}{h} + \frac{2-\sigma_v}{\sigma_v}(\mathrm{Kn}^2 - \mathrm{Kn})\right], \quad (8)$$

which is identical to the results obtained using the Eq. (1a) up to second-order terms in Kn given below:

$$U(y) = \frac{h^2}{2\mu}\frac{dP}{dx}\left[\frac{y^2}{h^2} - \frac{y}{h} - \frac{2-\sigma_v}{\sigma_v}\frac{\mathrm{Kn}}{1+\mathrm{Kn}}\right]. \quad (9)$$

This can be easily seen by expanding the last term in Eq. (9) as a geometric series expansion in terms of powers of Kn. However, it still contains nonphysical third- and higher-order corrections whereas the new approach gives exact results (within the physical model assumptions). The leading error in Eq. (9) is therefore proportional to $(h^2/2\mu)|(\partial P/\partial x)|\ \mathrm{Kn}^3$.

2.3 Summary of Computational Models. We summarize here, for convenience, all the computational models we have developed which are implemented in the spectral element code μFlow. This code can be used to analyze rarefaction, compressibility, viscous heating, and thermal creep effects and their relative importance. The current capabilities of these codes are summarized in Table 1.

Our incompressible models incorporate both the new (Eq. (4)) and the old boundary conditions (Eq. (1a)). There are no fundamental limitations in implementing the new boundary conditions for three-dimensional flows. The new boundary conditions have also been implemented in the version of incompressible flow solver, which solves the momentum equation only. In the following sections, we use the code μFlow to study in detail rarefaction and compressibility effects in gas microflows.

3 Shear-Driven Microflows

Shear-driven flows are encountered in micromotors and microbearings. In the simplest form, the linear Couette flow can be used as a prototype flow to model such flows driven by a moving plate. An analytical solution is easy to obtain given the simplicity of the geometry consisting of two plates separated by a distance h. The flow is driven by moving the upper plate at a constant velocity U_∞; the upper plate temperature is at T_∞ while the bottom plate is assumed to be adiabatic. Also for simplification, viscosity and thermal conductivity are assumed to vary linearly with temperature (i.e., $\kappa \sim \mu \sim T$), and the Prandtl number is fixed (for air $\mathrm{Pr} = 0.72$). For a no-slip Couette flow it is possible to obtain the friction coefficient ($C_f = \tau_w/(0.5\rho U_\infty^2)$) (Liepmann and Roshko, 1957; p. 313):

$$C_f = 2\frac{1 + \mathrm{Pr}\dfrac{\gamma-1}{3}\mathrm{M}_\infty^2}{\mathrm{Re}}, \quad (10)$$

where M_∞ is the Mach number based on the upper plate velocity and temperature, and Re is the Reynolds number based on the channel height h.

To validate the developed code μFlow, we have performed a series of simulations corresponding to top plate temperature $T_\infty = 300$ K and Reynolds number $\mathrm{Re} = 5$. The simulations are performed by using 9 elements with 6^{th} order polynomial expansions per direction in each element. The Mach number M_∞ is specified by varying the driving velocity of the top plate U_∞. Correspondingly, rarefaction effects are specified through the Knudsen number, since

$$\mathrm{Kn}_\infty = \frac{\sqrt{\pi\gamma/2}\,\mathrm{M}_\infty}{\mathrm{Re}}. \quad (11)$$

The variation of friction coefficient as a function of Mach number and corresponding Knudsen number is shown in Fig. 3. The friction coefficient of no-slip compressible flow increases quadratically in agreement with Eq. (10), well above the constant value of the corresponding incompressible flow. The no-slip compressible flow simulations match the theoretical results exactly. For rarefied flows, slip effects change the friction coefficient significantly. Compressible slip-flow results are denoted by open circles in Fig. 3; for the specified conditions they correspond to small deviations from the incompressible slip-flow results obtained from

$$C_f = \frac{2}{\mathrm{Re}}\left[\frac{1}{1 + 2\dfrac{2-\sigma_v}{\sigma_v}\mathrm{Kn}}\right]. \quad (12)$$

In linear Couette flow the pressure is constant and therefore compressibility effects are due to temperature changes only. As M_∞ increases the temperature difference between the two plates gets larger (due to the viscous heating). Correspondingly, compressibility effects become significant. It is seen in Fig. 3 that significant deviations from incompressible flows (slip/no-slip) are obtained for $\mathrm{M}_\infty > 0.3$. In particular, we investigated a case where the bottom plate is kept at $T_w = 350$ K while the top

Table 1 Flow models and boundary conditions implemented in the μFlow code

Flow type	B.C. type	2-D/3-D	V. Slip	T. Creep	T. Jump	Kn limit
Incomp 1	$\theta(Kn, Kn^2)$	2-D/3-D	Yes	Yes	Yes	<0.1
Incomp 2	$\theta(Kn^n)$	2-D	Yes	assigned	No	>0.1
Comp	$\theta(Kn^n)$	2-D	Yes	Yes	Yes	<0.5

plate is kept at T_∞ = 300 K. The friction coefficient of this case is also given in Fig. 3 (indicated as ΔT = 50 K). The simulation results are shown by solid and open triangles for the no-slip and the slip cases, respectively. The trend is different than the adiabatic bottom plate case. No-slip results show small variation of C_f as a function of M, while for slip flows C_f is reduced significantly as Kn is increased.

The density variation across the channel for compressible no-slip as well as slip flows is shown in Fig. 4 for the case with adiabatic bottom wall. Here, we have normalized the density variation by the top plate density of the no-slip case (solid line). The no-slip cases exhibit large density variations for relatively large values of M_∞. Since the pressure is constant, density variation across the channel is due to the drastic change in temperature, which is attributed to viscous heating effects. However, density variations are reduced in slip flows. There are two reasons for this behavior: First, the shear stress is reduced due to slip, reducing the viscous heating (work done by viscous stresses in the energy equation). Second, a temperature jump exists at the driving (top) plate; there is no temperature-jump on the bottom plate since it is adiabatic.

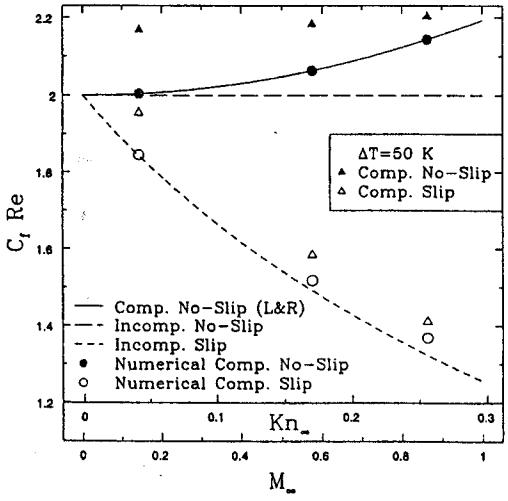

Fig. 3 Variation of skin friction as a function of M and Kn for Couette flow (Re = 5, T_∞ = 300 K)

The flow in a micromotor or a microbearing is more complicated than the linear Couette flow. We therefore consider a shear-driven grooved channel flow in order to model the geometric complexity of these microdevices. A segment of the domain is shown in Fig. 6. The flow separates and starts to recirculate in the grooves even for small Reynolds number flows. In our numerical model we have assumed that the top wall is moving with speed U_∞, and both surfaces are kept at the same temperature (300 K). We also assumed that the geometry repeats itself along the flow direction. Therefore the flow is periodic, and only a section of the channel is simulated. In our simulations the Reynolds number is fixed (Re = 5.0), and the Knudsen number is increased by decreasing the channel gap (and correspondingly the entire geometry is reduced by the same scale to ensure dynamic similarity of channels). Therefore the top wall speed U_∞ is increased to keep the Reynolds number constant, resulting in an increase of flow Mach number according to Eq. (11). The domain is discretized with 12 elements of 6th order polynomial expansions in each direction per element. The accuracy of the results was tested by increasing the order of polynomial expansions (p-refinement), and no significant changes in the results were observed.

In order to identify the accuracy of an incompressible model we compare the results of the incompressible model with the compressible model for the same Reynolds and Knudsen number. In Fig. 5 we present the variation of mass flow rate in the channel versus the drag on the top channel wall normalized with its no-slip incompressible counterpart. Drag reduction due to rarefaction is clearly seen. For example, for Kn = 0.128, about 30 percent drag reduction is observed. Both models predict a reduction in mass flow rate for slip flow. This is due to

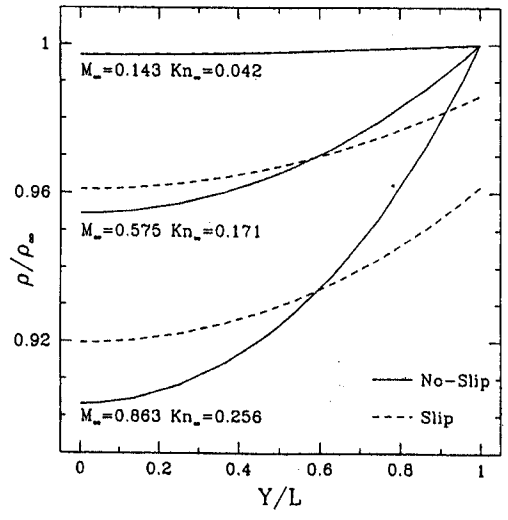

Fig. 4 Couette flow density variation across the channel for various values of M and Kn (Re = 5, T_∞ = 300 K)

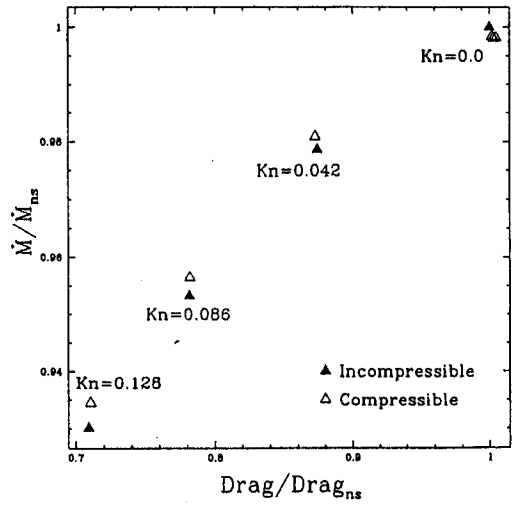

Fig. 5 Variation of mass flow rate versus drag force for the grooved channel, normalized with values of corresponding incompressible no-slip model

the reduction in the volumetric flow rate. The mass flow rate predicted by the incompressible model is less than that of the compressible one due to the inability of the incompressible model to predict variations in density.

The temperature contours for no-slip and slip (Kn = 0.086) flows are given in Fig. 6. The increase in temperature in the middle of the channel is due to viscous heating resulted from large shear stresses in this low Reynolds number flow. The viscous heating for slip flow is less than that of no-slip flow due to the reduction in shear stresses caused by the velocity slip. Also, the temperature of the gas near the walls is not the same with the prescribed wall temperature due to the temperature jump effects. This may create a problem for micro-gas-flow temperature measurements. Finally, the change in the temperature due to the viscous heating seems to be small in magnitude. However, in microflows the *gradients* in temperature can be quite large due to the small length scales even for one degree temperature difference.

4 Pressure-Driven Microflows

We consider here two-dimensional flow between parallel plates at a distance h, with L being the channel length, where $L/h \gg 1$. The flow is sustained by a pressure gradient dP/dx. We also assume that the Reynolds number is relatively low and that the Knudsen number $\mathrm{Kn} < 0.5$. It is therefore possible to simplify the Navier-Stokes equations for a uni-directional, isothermal flow by neglecting the inertial terms ($\rho u_j (\partial u_i/\partial x_j)$) in the governing equations. This results in the following analytical solution for the streamwise velocity profile,

$$U(y) = \frac{h^2}{2\mu}\frac{dP}{dx}\left[\frac{y^2}{h^2} - \frac{y}{h} + \frac{2-\sigma_v}{\sigma_v}(\mathrm{Kn}^2 - \mathrm{Kn})\right], \quad (13)$$

where we have used the new high-order boundary conditions (Eq. (4)). Notice that the second-order correction, which is typically omitted in other works (Arkilic et al., 1994), has the opposite sign compared to the first-order term; its contribution may be significant, especially for surfaces for which $\sigma_v < 1$.

The corresponding mass flow rate is computed from $\dot{M} = \rho \int_0^h U(y)dy$, where $\rho = P/RT$, assuming we can still treat the rarefied gas as an ideal gas. Expressing the Knudsen number at a location x as a function of the local pressure, i.e., $\mathrm{Kn} = \mathrm{Kn}_0 P_0/P$, where the subscript "0" refers to exit conditions, we obtain:

$$\dot{M} = \frac{h^3 P_0^2}{24\mu RTL}\left[(\Pi_i^2 - 1) + 12\frac{2-\sigma_v}{\sigma_v}(\mathrm{Kn}_0(\Pi_i - 1) - \mathrm{Kn}_0^2 \ln \Pi_i)\right], \quad (14)$$

where we have defined $\Pi_i \equiv P_i/P_0$ as the pressure ratio between inlet and exit. The corresponding flowrate without rarefaction is given by

$$\dot{M}_{ns} = \frac{h^3 P_0^2}{24\mu RTL}(\Pi_i^2 - 1). \quad (15)$$

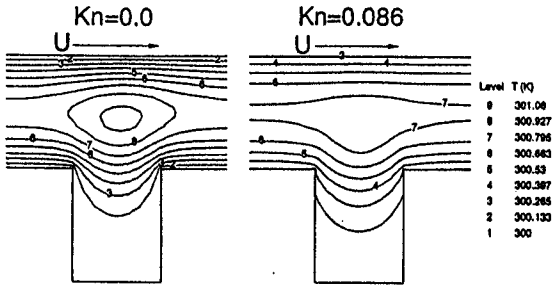

Fig. 6 Temperature contours in no-slip and slip grooved channel

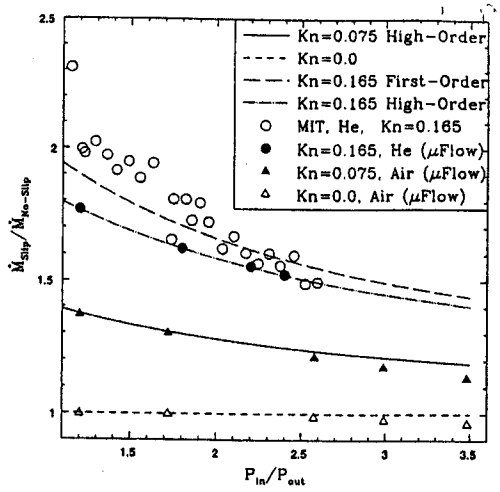

Fig. 7 Variation of mass flow rate normalized with the corresponding no-slip mass flow rate as a function of pressure ratio

Therefore, the increase in mass flow rate due to rarefaction can be expressed as

$$\frac{\dot{M}}{\dot{M}_{ns}} = 1 + 12\frac{2-\sigma_v}{\sigma_v}\frac{\mathrm{Kn}_0}{\Pi_i + 1} - 12\frac{2-\sigma_v}{\sigma_v}\mathrm{Kn}_0^2\frac{\ln \Pi_i}{\Pi_i^2 - 1}. \quad (16)$$

It is seen from this formula that the effect of the second-order correction is to reduce the increase in mass flow rate due to first-order slip. In other words, the often-used first-order velocity-slip boundary condition over-predicts the mass flowrate for a given pressure ratio Π_i.

Having obtained the mass flowrate, the corresponding pressure distribution along the channel can be easily obtained as

$$1 - \Pi^2 + 12\frac{1-\sigma_v}{\sigma_v}\mathrm{Kn}_0(1 - \Pi) + 12\frac{2-\sigma_v}{\sigma_v}\mathrm{Kn}_0^2 \ln(\Pi) = B(L - x), \quad (17)$$

where B is a constant such that $\Pi(0) = \Pi_i$. Here we have defined $\Pi(x) = P/P_0$, i.e., the pressure at a station x normalized with the exit pressure. The above equation provides an implicit relation for $\Pi(x)$; the pressure distribution for a first-order boundary condition is obtained explicitly by neglecting the second-order terms ($\mathcal{O}(\mathrm{Kn}^2)$) in Eq. (17).

The formula for the flow rate has been tested directly using experimental data reported by Arkilic et al. (1994) as well as simulation results obtained using our code μFlow. The results are plotted in Fig. 7 in terms of ratio of slip mass flow rate to the corresponding no-slip flow rate predicted by Eq. (16) as a function of pressure ratio. Microchannel helium flow experiments of Arkilic et al. (1994) show a maximum of 10 percent deviation from the first-order theoretical curve. The deviations are more significant especially for low pressure ratio cases. The gain in the mass flow rate due to slip effects is very significant but it is reduced as the pressure ratio is increased. Comparison of the high-order formula with the first-order formula shows about 8 percent deviations for small pressure ratios; the deviations are reduced for higher pressure ratio cases. The numerical predictions for helium flow are consistent with the high-order formula, validating the accuracy of Eq. (16) for helium flows up to the pressure ratios studied in this paper. Both the rarefied air flow (Kn = 0.075) and the no-slip air flow show deviations from the high-order formula especially for high pressure ratios.

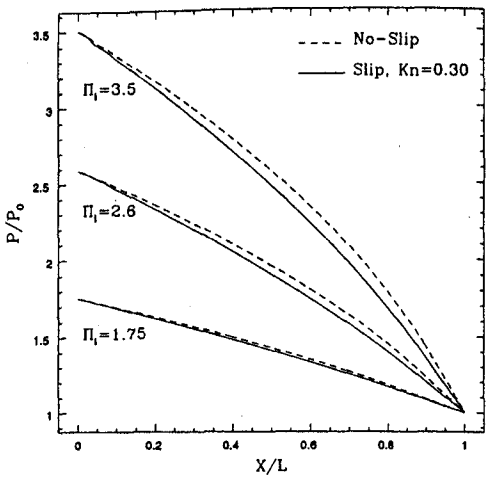

Fig. 8 Computed pressure distribution along the channel center for air flow (results are due to μFlow)

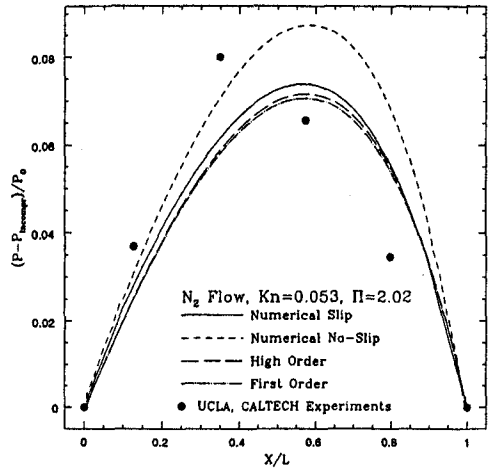

Fig. 10 Deviation from linear pressure drop for Π_i = 2.02, nitrogen flow, (h = 1.25 μm); circles correspond to experimental data by Liu et al. (1993)

The numerical predictions show less mass flow rate than the values predicted by the formula. The reason for this is the pronounced compressibility effects caused by the inertial terms in the Navier-Stokes equations, which were neglected in the derivation of Eq. (16).

Next we examine the pressure distribution along the channel; the experimental results by Liu et al. (1993) and Pong et al. (1994) show a nonlinear pressure distribution. In Fig. 8 we plot the pressure distribution for air flow for different values of pressure ratios (Π_i) obtained from simulation. Also included is the pressure distribution for the corresponding compressible, no-slip flows. The curvature in the pressure distribution is more pronounced for the no-slip compressible flows than the rarefied flows, and this effect gets more dominant as the pressure ratio (Π_i) is increased. For cases with $\Pi_i \leq 1.75$, the pressure drop is practically linear, resembling an incompressible flow.

To investigate the compressibility and rarefaction effects further, deviations from linear pressure distribution for helium and air flows for pressure ratio $\Pi_i = 3.5$ is given in Fig. 9. Here we see that unlike the experimental findings of Liu et al. (1993) and Pong et al. (1994) the curvature in the pressure distribution for helium is less pronounced compared to the air microflow. This trend should be expected since for the same pressure ratio and exit pressure, the local Mach number for helium flow is smaller than the Mach number for air flow. Also the rarefaction effects for helium flow is larger than that of the air flow due to the relatively large mean free-path of helium molecules compared to air. Our simulation results indicated that rarefaction causes the opposite effect than compressibility, which is also evident from the analytical expression (Eq. (17)). This is shown in Fig. 10 where we plot the analytical predictions taking into account first- and second-order Knudsen number effects. The simulation results for nitrogen flow of Kn = 0.156, corresponding to the experiments of Liu et al. (1993), are also included. We see that pressure distribution agrees with the high-order curve. The discrepancies are due to the neglected inertial terms in Eq. (17). The trends of experimental data and the simulations are qualitatively the same. They both predict smaller deviations from linear pressure drop than the corresponding no-slip flow. There are, however, quantitative differences such as the maximum deviation location from linear pressure drop, which is at $X/L \simeq 0.4$ for the experiments, and $X/L \simeq 0.55$ for the simulation. We observed a larger disagreement with the "second generation" experimental data obtained by Pong et al. (1994). Because of current uncertainties in these measurements (a different pressure distribution is measured if the flow direction is reversed) we have not included this comparison in the present paper.

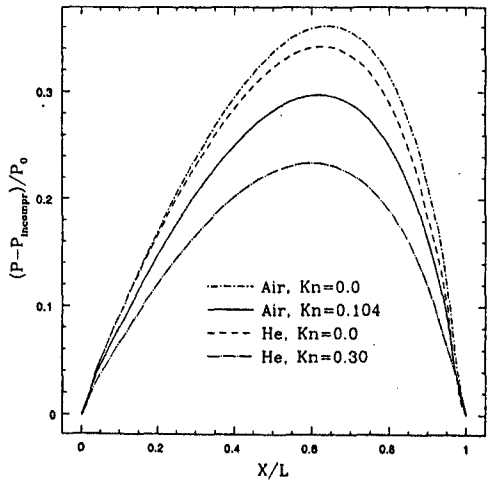

Fig. 9 Deviation from linear pressure drop for air and helium flows (h = 0.65 μm, Π_i = 3.5, P_{out} = 1 atm). Results are due to μFlow)

Before we end this section, we would like to comment on the limitations of the analytic formulas given in (14) and (15). The derivation of these formulas is based on the additional assumptions that density and pressure across the channel at any given location are constant. Thermal effects are also neglected. Due to these limitations the analytic formulas can be applied to low Mach number flows (typically $M_0 \leq 0.10$). In our simulations we have computed non-negligible density variations across the channel, especially for large pressure drop of nitrogen and air flows. The importance of inertial terms compared to the cross flow diffusion terms ($\simeq \mathrm{Re}(h/L)$) is estimated by using the aspect ratio $L/h = 20$, and the Reynolds number obtained by μFlow. The difference between the analytic predictions and the solution of full Navier-Stokes equations is expected to be less than 20% for the most severe cases simulated in this paper. Equation (15) is indeed similar to an incompressible model where $(dP/dx) = (P_{in} - P_{out})/L$, and density is evaluated at average pressure in the channel (i.e., $\rho_{av} = ((P_{in} + P_{out})/2)/RT$).

5 Proposed Benchmark Experiments

There are several difficulties in performing microflow experiments. First, the mass flow rate is quite small ($10^{-13} \sim 10^{-12}$

kg/s) and therefore difficult to measure. Second, pointwise measurements of pressure and temperature are difficult to make; the only pressure distribution obtained experimentally so far is due to Liu et al. (1993). Finally, the size and shape of microchannels are difficult to characterize. In the following, we introduce ideas for specific experiments that can alleviate some of these difficulties. The primary objective is the generation of accurate data bases for validating predictive computational models for gas microflows, and developing absolute standards for measurements.

Pressure-Driven Microflow. The purpose of this experiment is to measure and correlate the mass flowrate and pressure drop in microchannel flows. The pressure distribution in the channels should also be measured to identify compressibility effects. A critical aspect of this benchmark experiment is the ability to modify and characterize the microchannels. Many different channel cross-sections, such as rectangular as well as triangular (in the shape of V-grooves) should be etched. Before the final assembly of the channels, surface characteristics, shape and dimensions of the channels should be accurately measured. The purpose of using various channel cross-sections in these benchmark experiments is to develop the concept of the equivalent "hydraulic diameter" for unified pressure drop predictive models like the Moody diagram in large diameter pipes (Schlichting, 1979).

We propose to perform pointwise pressure measurements by connecting the tap holes on microchannels to a micro-measurement system. The micro-measurement system we propose consists of two volumes separated by a thin, flexible diaphragm, which provides a sensitive measure of the pressure difference between the pressure of two chambers it separates. This provides comparison of pressure in a micro-volume (connected to the microchannels), with a large, and hence easily measured volume of fluid (measurement chamber). The curvature and deflection of the diaphragm will be measured optically, the pressure in the measurement chamber will be adjusted till the deflection of the diaphragm vanishes (i.e., the pressure on both sides of the diaphragm are identical), and the pressure at the measurement chamber will be directly recorded. Our approach of measuring point wise pressure in microchannels differs from that of Liu et al. (1993), where micro-pressure sensors are manufactured adjacent to the microchannels. The proposed measurement system here, is based on pressure measurements of much larger volume of fluids, and therefore it is expected to be more accurate than the measurement system used by Liu et al. (1993) and Pong et al. (1994).

Shear-Driven Microflow. The purpose of this experiment is to study the rarefaction effects without the adverse effects of compressibility, which are present in pressure-driven microchannel flows. Here we consider a device similar to the Taylor-Couette device. The flow is driven by one of the surfaces of the channels which is moving along the flow direction. The inner cylinder is rotated at a prescribed rate; the corresponding torque balancing the shear stress on the inner surface is measured. The gap between two cylinders should be kept in the order of a micron. The cylinder radius and height should be a few centimeters; this is necessary for the validity of "thin gap" approximation. Maximizing the flow surface has several advantages, e.g., more reliable data can be obtained as the magnitude of the torque will be large, and the end-effects can be neglected. The micro-Taylor-Couette device is conceptually a large-scale device with micron-scale flow gap. Therefore, making such a device does not require fabrication techniques used in MEMS.

Compressibility can be neglected for moderate rotational speeds. However, increase in the rotational speed results in significant compressibility and viscous heating effects. The experiments should be performed in a temperature and pressure controlled environment. Preferably one of the cylinder surface should be insulated, and cylinder surface temperature and pressure should also be measured. This way, compressibility and viscous heating effects can be identified. One other advantage of performing the experiments in a pressure-controlled environment is the ability to vary the Knudsen number by either adjusting the pressure in the apparatus or changing the gas.

6 Summary

In this paper, we have investigated the combined effects of compressibility and rarefaction in gas microflows. The flow regime we have considered corresponds to slip-flow, with the Knudsen number $Kn \leq 0.3$. The geometry we have primarily considered is a flat channel in order to compare with available experimental results and approximate theoretical models. However, the numerical models we have developed are appropriate for complex geometries such as the grooved microchannel flow that we modeled in Section 3. Complex geometries are of great interest due to their practical use in fabricating channel networks in micro-scales consisting of sudden expansions and contractions, bends, branches, etc. (Zohar, 1994).

For pressure-driven channel flows, we have found that a nonlinear pressure distribution is established in microchannels in accordance with the experimental results of Liu et al. (1993). In particular, for large pressure drop in air or nitrogen flow, compressibility effects are dominant and the curvature in the pressure distribution plot is very pronounced. However, in more rarefied flows such as helium flow, a pressure distribution with smaller curvature is obtained. In other words, our simulation results as well as approximate analytical models suggest that *rarefaction negates compressibility,* in contrast with experimental findings of Pong et al. (1994).

We have demonstrated that compressibility for shear-driven flows is negligible, and thus rarefaction dominates the momentum and energy transport. In particular, drag-reduction experienced in micro-devices can be clearly explained by rarefaction effects. Also, viscous heating effects is observed to create considerable temperature gradients in micron-sized domains even for iso-thermal boundary conditions.

Based on the studies presented here we have proposed a set of benchmark experiments designed to validate the slip-flow theory in modeling microflows. In particular, we focus on the combined rarefaction and compressibility effects and suggest specific pressure distribution and mass flowrate measurements in microchannels of various crossections. In addition, we propose a new experiment isolating rarefaction effects only by measuring the shear stress (torque) in a micro-Taylor-Couette device. These experiments are also intended for the experimentalists to perform metrology experiments and establish secondary standards. Moreover, the results of these experiments will be valuable to groups developing CAD systems for micromechanical research and development.

Acknowledgments

We are very grateful to S. A. Tison of NIST, C. M. Ho of UCLA and K. Breuer of MIT for making their experimental data available to us. This work was supported by NSF grant ECS-90-23760 under the supervision of Dr. George Lea.

References

Arkilic, E., Breuer, K. S., and Schmidt, M. A., 1994, "Gaseous Flow in Microchannels," ASME, FED-Vol. 197, *Application of Microfabrication to Fluid Mechanics,* pp. 57–66, ASME.

Beskok, A., and Karniadakis, G. E., 1992, "Simulation of Slip-Flows in Complex Micro-Geometries," ASME, DSC-Vol. 40, pp. 355–370.

Beskok, A., and Karniadakis, G. E., 1993, "Simulation of Heat and Momentum Transfer in Complex Micro-Geometries," AIAA Shear Flow Conference July 6–9, Florida, AIAA 93-3269.

Beskok, A., and Karniadakis, G. E., 1994, "Simulation of Heat and Momentum Transfer in Complex Microgeometries," *AIAA J. Thermophysics & Heat Transfer,* Vol. 8 (4), pp. 647–655.

Beskok, A., and Karniadakis, G. E., 1996, "A Spectral Element Method for Subsonic Viscous Flows," in progress.

Bryzek, J., Petersen, K., and McCulley, W., 1994, "Micromachines on the March," *IEEE Spectrum*, pp. 20–31.

Gabriel, K., Javris J., and Trimmer W., 1988, "Small Machines, Large Opportunities," Technical report, NSF.

Harley, J. C., Huang, Y., Bau, H. H., and Zemel, J. N., 1995, "Gas Flow in Micro-Channels," *Journal of Fluid Mechanics*, Vol. 284, pp. 257–274.

Howe, R. T., Muller R. S., Gabriel, K. J., and Trimmer W. S., 1990, "Silicon Micromechanics: Sensors and Actuators on a Chip," *IEEE Spectrum*, pp. 29–35.

Kennard, E. H., 1938, *Kinetic Theory of Gasses*, McGraw-Hill, New York.

Knudsen, M., 1909, "Die gesetze der molekularströmung und der inneren riebungsströmung der gase durch röhnen," *Ann. Phys*, Vol. 33, pp. 75–130.

Kruger, A. J., Larmit, A. J. F., and de Wit, M. H., 1970, "Flow of a Rarefied Gas Through a Long Capillary (Cylindrical or Bounded by Planes) Generated by a Temperature Gradient," Proc. 7th *Int. Symp. on Rarefied Gas Dynamics*, pp. 1015–1022.

Liepmann, H. W., and Roshko, A., 1957, *Elements of Gas Dynamics*, Wiley.

Liu, J. Q., Tai, Y. C., Pong, K. C., and Ho, C. M., 1993, "Micromachined Channel/Pressure Sensor Systems for Micro Flow Studies," 7th Int. Conf. on Solid-State Sensors and Actuators, pp. 995–998, Transducers '93.

Loyalka, S. K., and Hamoodi, S. A., 1990, "Poiseuille Flow of a Rarefied Gas in a Cylindrical Tube: Solution of Linearized Boltzmann Equation," *Phys. Fluids A*, Vol. 2 (11), pp. 2061–2065.

Mehregany, M., Nagarkar, P., Senturia, S. D., and Lang, J. H., 1990, "Operation of Microfabricated Harmonic and Ordinary Side-Drive Motor," IEEE Micro Electro Mechanical System Workshop, Napa Valley, CA.

Muntz, E. P., 1989, "Rarefied Gas Dynamics" *Ann. Rev. Fluid Mech.* Vol. 21, pp. 387–417.

O'Connor, L., 1992, "MEMS: Microelectromechanical Systems," *Mechanical Engineering*, Vol. 114, No. 2, pp. 40–47.

Pfahler, J., Harley, J., Bau, H. H., and Zemel, J., 1991, "Gas and Liquid Flow in Small Channels," ASME, Vol. 32, pp. 49–59.

Pong, K. C., Ho, C. M., Liu, J., and Tai, Y. C., 1994, "Non-linear Pressure Distribution in Uniform Microchannels," ASME, FED-Vol. 197, *Application of Microfabrication to Fluid Mechanics*, pp. 51–56, ASME.

Reed, M. L., 1993, "Near Term Applications of Microelectromechanical Systems," *4th International Symposium on Micro Machine and Human Science*, Nagoya, Japan, pp. 77.

Saxena, S. C., and Joshi, R. K., 1981, "Thermal Accommodation and Adsorption Coefficients of Gasses," Vol. 1, 2, Series Editors Y. S. Touloukian, C. Y. Ho, McGraw-Hill/CINDAS Data Series On Material Properties, McGraw-Hill, New York.

Schaaf, S. A., and Chambre, P. L., 1961, *Flow of Rarefied Gases*, Princeton University Press, Princeton, NJ.

Schlichting, H., 1979, *Boundary-Layer Theory*, 7th ed., McGraw-Hill, New York.

Shoji, S., and Esashi, M., 1994, "Microflow Devices and Systems," *Journal of Micromechanics and Microengineering*, Vol. 4 no 4, pp. 157–171.

Tai, Y. C., Fan, L. S., and Muller, R. S., 1989, "IC-processed micro-motors: design, technology, and testing," *IEEE Micro Electro Mechanical System Workshop*, Salt Lake City, Utah.

Thompson, S. L., and Owens, W. R., 1975, "A Survey of Flow at Low Pressures," *Vacuum*, Vol. 25, pp. 151–156.

Tison, S. A., 1993, "Experimental Data and Theoretical Modeling of Gas Flows Through Metal Capillary Leaks," *Vacuum*, Vol. 44, pp. 1171–1175.

Tison, S. A., 1994, Private communications.

Wilding, P., Pfahler, J., Zemel, J. N., Bau, H. H., and Kricka, L. J., 1994, "Manipulation and Flow of Biological Fluids in Straight Channels Micromachined in Silicon," *Clinical Chemistry*, Vol. 40, No. 1, pp. 43–47.

Zengerle, R., and Richter, M., 1994, "Simulation of Microfluid Systems," *Journal of Micromechanics and Microengineering*, Vol. 4, No. 4, pp. 192–204.

Zohar, Y., 1995, Private communications.